applied sciences

MDPI

Article

Numerical Modelling of High-Speed Loading of Periodic Interpenetrating Heterogeneous Media with Adapted Mesostructure

Alexander Kraus, Andrey Buzyurkin, Ivan Shabalin and Evgeny Kraus *

Khristianovich Institute of Theoretical and Applied Mechanics SB RAS, Novosibirsk 630090, Russia; akraus@itam.nsc.ru (A.K.); buzjura@itam.nsc.ru (A.B.); shabalin@itam.nsc.ru (I.S.)
* Correspondence: kraus@itam.nsc.ru

Abstract: A series of calculations has been conducted to study the high-speed interaction of space debris (SD) particles with screens of finite thickness. For the first time, taking into account the fracture effects, a numerical solution has been obtained for the problem of high-velocity interaction between SD particles and a volumetrically reinforced penetrating composite screen. The calculations were performed using the REACTOR 3D software package in a three-dimensional setup. To calibrate the material properties of homogeneous screens made of aluminum alloy A356, stainless steel 316L, and multilayer screens, methodical load calculations were carried out. The properties of materials have been verified based on experimental data through systematic calculations of the load on homogeneous screens made of aluminum alloy A356, stainless steel 316L, and multilayer screens comprising a combination of aluminum and steel plates. Several options for the numerical design of heterogeneous screens based on A356 and 316L were considered, including interpenetrating reinforcement with steel inclusions and a gradient distribution of steel throughout the thickness of an aluminum matrix. The study has revealed that the screens constructed as a two-layer composite of A356/316L, volumetrically reinforced composite screens, and heterogeneous screens with a direct gradient distribution of steel in the aluminum matrix provide protection for devices from both a single SD particle and streams of SD particles moving at speeds of up to 6 km/s. SD particles were modeled as spherical particles with a diameter of 1.9 mm made of the aluminum alloy Al2017-T4 with a mass of 10 mg.

Keywords: heterogeneous material; reinforcement; high-speed interaction; barrier of finite thickness; space debris

check for updates

Citation: Kraus, A.; Buzyurkin, A.; Shabalin, I.; Kraus, E. Numerical Modelling of High-Speed Loading of Periodic Interpenetrating Heterogeneous Media with Adapted Mesostructure. *Appl. Sci.* **2023**, *13*, 7187. https://doi.org/10.3390/app13127187

Academic Editor: Jérôme Morio

Received: 26 April 2023
Revised: 9 June 2023
Accepted: 13 June 2023
Published: 15 June 2023

Copyright: © 2023 by the authors. Licensee MDPI, Basel, Switzerland. This article is an open access article distributed under the terms and conditions of the Creative Commons Attribution (CC BY) license (https://creativecommons.org/licenses/by/4.0/).

1. Introduction

Man-caused pollution of near-Earth space poses a threat to spacecraft, including the real risk of damage and destruction. The term "space debris" (SD) appeared in the late 1980s and, according to Flury's definition [1], describes all artificial objects and their parts in near-Earth space that do not serve any useful purpose or function. Since the launch of the first artificial Earth satellite, the number of launches has increased, resulting in the accumulation of both large fragments and small SD particles [2].

The collision of spacecraft construction elements with SD may lead to catastrophic consequences or local damage resulting in a loss of efficiency or function. In addition, natural meteoric particles from distant space pose a threat. The longer the spacecraft is in flight, the greater the probability of a collision with SD particles. To ensure effective protection against various external influences, the spacecraft's body must be technologically advanced in production and have the smallest possible mass. For low-orbit spacecraft, designing hulls and protective screens is particularly relevant due to the concentration of a large number of SD on low orbits.

Several types of screens have been developed to protect against SD particles. Whipple's protection [3] is an innovative approach that prevents impacts by incorporating a large

number of thin shells that destroy incoming kinetic energy particles. This creates a cloud of fragments that dissipate the kinetic energy of impact and distribute it over a larger area [4]. Multilayer heterogeneous screens are another type of protective construction that weakens the impact impulse through multiple reflections on multiple boundaries [5]. Other protective constructions, such as porous structures [6] and woven composites [7], have gaps in material properties that contribute to the dissipation of impact energy and prevent its spread. However, these protection technologies are often bulky, which presents a challenge in the design of aerospace systems where size and weight are severely limited. To sum up, the challenge of reducing the mass of spacecraft protective screens while maintaining their effectiveness remains a significant concern.

Since the dawn of the space era, composites based on organic matrices and metal matrices (MMC) have been developed for use in space. These materials possess high specific stiffness and a virtually zero coefficient of thermal expansion (CTE). Organic matrix composites, such as graphite/epoxy resin, have been used in the space for truss elements, paneling, antennas, waveguides, and parabolic reflectors. On the other hand, MMCs are able to withstand high temperatures and possess high thermal conductivity, low CTE, high specific stiffness, and strength. These potential advantages generated optimism regarding the use of MMCs in critical space systems in the late 1980s [8].

The successful development of many modern branches of technology is primarily associated with the utilization of cutting-edge materials in construction, certain parts of which are subjected to extreme loads due to various reasons. Making an appropriate choice of a material capable of enduring the applied stress over a specific period of time can be quite laborious without conducting a theoretical prediction. The stress–strain and thermodynamic calculations of the loaded material, in the hands of an experienced researcher, serve as the key to enhancing reliability and prolonging the lifespan of the entire structure.

The advancement and refinement of material creation technologies with predetermined properties, such as additive technologies, electron beam welding, and so on, have broadened the scope of heterogeneous materials' applications. Experimental work focused on practically developing manufacturing technologies for such heterogeneous mediums with specific properties far surpasses the methods used for predicting the properties themselves. Consequently, there now exists a significant gap between the practical implementation of complex heterogeneous materials and the level of knowledge concerning the properties of such materials under intense dynamic loads.

The development of additive manufacturing technologies for the production of structural elements stimulates new approaches to designing materials and products [9–13]. One of the current challenges at the intersection of mechanics, materials science, and physics is the development of methods and approaches for designing products with a certain material structure that provides the required functional and structural properties.

In mechanical engineering, there is a task to increase the strength and damping properties of metals, which often contradict each other. Additively manufactured interpenetrating composites are a new type of "metal-metal" composites for use in high-energy absorption systems. In this system, the matrix phase—a liquid metal with a melting temperature lower than the melting temperature of the lattice—is poured into the reinforcing phase with a continuous lattice configuration made additively. The result is a periodically interpenetrating composite in which each component forms a continuous network. Studies of such materials show that the boundary between the reinforcing and matrix phases can demonstrate significantly different mechanical properties of the composite, which allows for the dissipation of the impact energy.

For example, ref. [14] proposed a method for creating an Mg-NiTi composite with a bicontinuous architecture of an interpenetrating heterogeneous medium. For this, a magnesium melt is infiltrated into a three-dimensionally printed nitinol frame, which allows for the creation of a composite with a unique combination of mechanical properties: increased strength at various temperatures, remarkable damage resistance, good damping ability at

various amplitudes, and exceptional energy absorption efficiency. After deformation, the shape and strength of the composite can be restored by thermal treatment.

Our scientific interest was sparked by an experiment studying the response of a heterogeneous medium with an adapted interpenetrating mesostructure. This mesostructure was fabricated using the hybrid additive technology known as PrintCast [15–17]. The experiment focused on investigating the impact loads that arise during high-velocity interactions, which can be utilized as one of the spacecraft protection options [18]. The results of the experiment demonstrated that the composite made of stainless steel 316L and aluminum alloy A356 using PrintCast technology is more resistant to delamination than monolithic screens made of the same materials. The studies have shown that the metal matrix composite with an adapted interpenetrating mesostructure is a promising system for spacecraft protection in cases where size limitations prevent the use of traditional protection methods. The heterogeneous mesostructure of this composite leads to a significant attenuation of the shock wave by multiple scattering at the interfaces of dissimilar materials and prevents macroscopic spall [19].

In work [20], the mechanical properties of PrintCast composites and their dependence on the volume fraction of reinforcement with steel 316L were studied. Uniaxial tensile tests were conducted on A356/316L PrintCast composites containing 30%, 40%, and 50% reinforcement. An increase in ductility by 200% and absorbed energy by 400% was observed when the volume fraction of reinforcement increased from 30% to 40%. However, with an increase in reinforcement from 40% to 50%, a much smaller increase in these parameters was observed. The sample with a volume fraction of 30% failed due to localized deformation in a single area after the onset of failure, unlike the samples with volume fractions of 40% and 50%, where the failure occurred due to non-localized damage throughout the cross-section of the sample.

The authors proposed the technology of direct numerical construction of heterogeneous media in [21,22], and comprehensive studies were conducted to determine the parameters in heterogeneous media, demonstrating their possible advantages. The works include comparisons with experimental data as well as descriptions of some mixture laws and methodologies for working with them. The work in [23] showed that during the propagation of an impulse in all media, it evolves into an elastic stress–strain state where its amplitude and length no longer depend on the distance traveled. Studies were also conducted on the influence of inclusion sizes. It was found that for heterogeneous materials with large inclusions, the rate of attenuation of the impulse amplitude is significantly higher compared to heterogeneous materials with small inclusions. Reducing the overall concentration of ceramics from 40% to 20% volume fraction in the heterogeneous material preserves all trends in the behavior of a short impulse during its propagation through an obstacle.

2. Mathematical Problem Statement

The software package “REACTOR 3D” [24] was used to perform the calculations. The Lagrangian approach is commonly employed to describe the dynamic interaction of deformable solids as it provides a suitable framework for characterizing the behavior of the medium. The region containing the composite is covered by a finite difference grid, where triangular-shaped cells fill the space without gaps or overlaps. Each triangular cell is assigned its own material’s physical and mechanical properties. When transitioning from one cell to another, the characteristics can change abruptly. The boundaries of the cells satisfy conditions for the collective motion of the heterogeneous material components. Inside the cells, the investigated quantities are determined using an explicit finite difference scheme.

2.1. The Main Conservation Laws

The mathematical formulation is described in [22,25,26]. The partial differential equations are converted to an explicit difference scheme on the difference grid along the trajectory of each material particle. The procedure for constructing the difference scheme is

described in detail elsewhere [25,26]. We use the system of equations for the deformable solid model, which includes the following equations:

– The particle trajectory equation

$$\dot{x}_i = u_i; \tag{1}$$

– The mass balance equation

$$V_0\rho_0 = V\rho; \tag{2}$$

– The momentum balance equation

$$\rho\dot{u}_i = \sigma_{ij,j}; \tag{3}$$

– The internal energy balance equation

$$\rho\dot{e} = \sigma_{ij}\dot{\varepsilon}_{ij}; \tag{4}$$

$\dot{\varepsilon}_{ij}$ is the strain rate tensor:

$$\dot{\varepsilon}_{ij} = \frac{1}{2}(u_{i,j} + u_{j,i}); \tag{5}$$

σ_{ij} is the stress tensor:

$$\sigma_{ij} = -\delta_{ij}P + s_{ij}; \tag{6}$$

where s_{ij} is the stress deviator, which characterizes the shear-induced change in the shape of a material particle; δ_{ij} is the Kronecker symbol.

The elastoplastic flow equations are formulated in the form of Prandtl–Reuss equations.

$$\hat{s}_{ij} + d\lambda' s_{ij} = 2G\dot{\varepsilon}'_{ij},\ \dot{\varepsilon}'_{ij} = \dot{\varepsilon}_{ij} - \dot{\varepsilon}_{kk}/3, \tag{7}$$

with the Huber–von Mises plasticity condition

$$s_{ij} \cdot s_{ij} \le 2 \cdot Y_0^2/3, \tag{8}$$

where Y_0 is the dynamic yield stress. Instead of calculating the scalar factor $d\lambda'$, we use the well-known procedure of reducing the stress deviator components to the yield circle [26]. In Equations (1)–(8), each of the subscripts i, j takes values 1, 2, and 3; summation is performed over repeating indices; a dot above a symbol denotes the time derivative, and a subscript after a comma denotes the derivative with respect to the corresponding coordinate; x_i and u_i are the components of the position and velocity vectors of a material particle, respectively; ρ is the current density; G is the shear modulus.

2.2. The Equation of State

A few-parameter equation of state in the form of the Mie–Gruneisen equation [27,28] is used

$$P = P_x + \frac{\gamma(V)c_{v,l}T}{V} + \frac{c_{v,e}T^2}{3V(V/V_0)^{2/3}}.$$

Here, P_x is the pressure on the zero isotherm; T is the temperature; $c_v = c_{v,l} + c_{v,e}$ is the constant-volume heat capacity equal to the sum of the lattice and electronic heat capacities; V and V_0 are the current and initial specific volumes; $\gamma(V)$ is the Gruneisen coefficient.

2.3. The Boundary Conditions

Each body in the Cartesian coordinate system $\{x_j\}$ corresponds to a computational domain $\mathrm{D}^i(\mathbf{x}, t)$ with boundaries $\mathrm{G}^i(\mathbf{y}, t)$ (see Figure 1). Here, $\mathbf{x} = \mathbf{x}(t)$ is the position

vector of the material particle and $\mathbf{y}$ are the boundary points. In the general case, the computational domains $\mathrm{D}^i(\mathbf{x}, \mathrm{t})$ change in time and can be multi-connected.

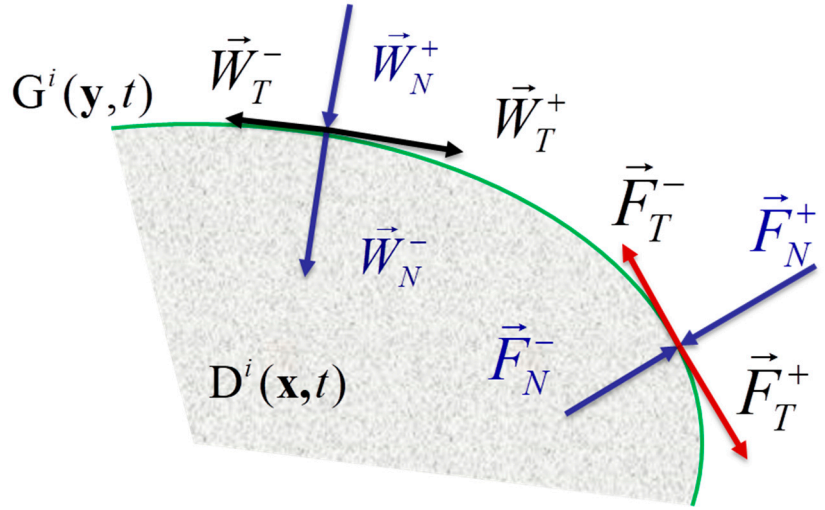


Figure 1. Boundary conditions.

The initial conditions for the i-th body at $t = 0$ in the region $\mathrm{D}^i(\mathbf{x}, \mathrm{t})$ are of the form:

$$\rho^i(\mathbf{x}, 0) = \rho^{i0}(\mathbf{x}),\ u_j^i(\mathbf{x}, 0) = u_j^{i0}(\mathbf{x}),\ s_{ij} = P = e = 0,$$

where $\rho^{i0}(\mathbf{x})$ and $u_j^{i0}(\mathbf{x})$ are the given initial distributions of the material density and the velocity vector over the area $\mathrm{D}^i(\mathbf{x}, \mathrm{t})$.

To formulate the boundary conditions, let us introduce the following notations:

- $\mathbf{n}^i$ the vector of the outward normal to the boundary $\mathrm{G}^i(\mathbf{y}, t)$ of the domain $\mathrm{D}^i(\mathbf{x}, \mathrm{t})$;
- $F^i(\mathbf{y}, t)$ the vector of external surface forces on the boundary $\mathrm{G}^i(\mathbf{y}, t)$;
- $W^i(\mathbf{y}, t)$ the vector of velocity at the boundary. $\mathrm{G}^i(\mathbf{y}, t)$.

The following conditions can be specified on any boundary of the domain $G^i(\mathbf{y}, t)$:

- kinematic

$$\mathbf{u}^i(\mathbf{y}, t) = W^i(\mathbf{y}, t),$$

- dynamic

$$\sigma_{kl}^i(\mathbf{y}, t)\ n_l^i = F_k^i(\mathbf{y}, t),\ (k, l = 1,\ 2,\ 3),$$

where σ_{kl}^i are the components of the stress tensor on the boundary of the domain $\mathrm{G}^i(\mathbf{y}, t)$, which typically needs to be determined;

- mixed

$$\mathbf{u}^i(\mathbf{y}, t) = W^i(\mathbf{y}, t),\ \mathbf{y} \in \mathrm{G}^{i\alpha}(\mathbf{y}, t),\ \sigma_{kl}^i(\mathbf{y}, t) n_l^i = F_k^i(\mathbf{y}, t), \mathbf{y} \in \mathrm{G}^{i\beta}(\mathbf{y}, t),\ \mathrm{G}^i(\mathbf{y}, t) = \mathrm{G}^{i\alpha}(\mathbf{y}, t) \cup \mathrm{G}^{i\beta}(\mathbf{y}, t).$$

The contact surface between two bodies $\mathrm{G}^{ij}(\mathbf{z}, t)$ is defined as the set of points $\mathbf{z}$ that satisfy the condition.

$$\mathrm{G}^{ij}(\mathbf{z}, t) = \mathrm{G}^i(\mathbf{y}, t) \cap \mathrm{G}^j(\mathbf{y}, t).$$

Certain compatibility conditions must be satisfied on the contact boundary between the bodies for the vectors of velocities $\mathbf{u}^i(\mathbf{z}, t)$ and $\mathbf{u}^j(\mathbf{z}, t)$, as well as the components of the stress tensor σ_{kl}^i and σ_{kl}^j. Specific types of conditions on the contact boundaries will be stated below. To simplify the algorithm for calculating the motion of the boundaries, we will use the external surface force vectors $F^i(\mathbf{y}, t)$. The reaction forces, which are determined during the problem-solving process, will be denoted by $\mathbf{R}^i(\mathbf{z}, t)$.

Let us assume that at each point $\mathbf{z}$ on the contact surface $G^{ij}(\mathbf{z},t)$, there exists a common normal. In this case,

$$\mathbf{n}^i = -\mathbf{n}^j.$$

Let us decompose the vector $\mathbf{A}(\mathbf{z},t)$ at point $\mathbf{z}$ into its normal $\mathbf{A}_n$ and tangential $\mathbf{A}_t$ components

$$\mathbf{A} = \mathbf{A}_n + \mathbf{A}_t. \tag{9}$$

These components can be calculated using the formulas.

$$\mathbf{A}_n = (\mathbf{A},\mathbf{n})\cdot\mathbf{n}, \quad \mathbf{A}_t = \mathbf{n}\times(\mathbf{n}\times\mathbf{A}).$$

Let us replace the action of body i on body j at point $\mathbf{z}$ with the reaction force vector $\mathbf{R}^i(\mathbf{z},t)$, and, correspondingly, the action of body j on body i with the reaction force vector $\mathbf{R}^j(\mathbf{z},t)$. Then, $\mathbf{R}^i(\mathbf{z},t) = -\mathbf{R}^j(\mathbf{z},t)$, and according to (9), we will have

$$\mathbf{R}^i = \mathbf{N}^i + \mathbf{T}^i,$$

where $\mathbf{N}^i$ and $\mathbf{T}^i$ are the normal and tangential components of the reaction force vector, respectively.

Let us consider the formulation of boundary conditions on the contact surface in specific cases:

- Ideal mechanical contact: The material particles belonging to the boundaries of the interacting bodies move as a single entity.

$$\mathbf{u}^i(\mathbf{z},t) = \mathbf{u}^j(\mathbf{z},t),\ \mathbf{R}^i(\mathbf{z},t) = -\mathbf{R}^j(\mathbf{z},t); \tag{10}$$

- Frictionless sliding: In this case, the conditions of non-penetration and equilibrium hold for the normal components of the reaction forces.

$$\mathbf{u}^i_{\mathbf{n}}(\mathbf{z},t) = \mathbf{u}^j_{\mathbf{n}}(\mathbf{z},t), \quad \mathbf{N}^{\mathbf{i}}_{\mathbf{n}}(\mathbf{z},t) = -\mathbf{N}^j_{\mathbf{n}}(\mathbf{z},t), \quad \mathbf{T}^i(\mathbf{z},t) = \mathbf{T}^j(\mathbf{z},t) = 0, \quad \mathbf{z}\in G^{ij}(\mathbf{z},t); \tag{11}$$

Condition (11) is applied only for compressive reaction forces, i.e., $(\mathbf{N}^i,\mathbf{n}^i) < 0$. If this condition is violated, stress-free surface conditions are applied to the boundaries $G^i(\mathbf{y},t)$ and $G^j(\mathbf{y},t)$.

- Sliding with Coulomb friction: Let the friction coefficient be k. The friction force is determined by the expression,

$$\mathbf{T}^i = \kappa\left|\mathbf{N}^i\right|\mathbf{q}^i,\ \mathbf{q}^i = -\frac{\mathbf{u}^i_t - \mathbf{u}^j_t}{\left|\mathbf{u}^i_t - \mathbf{u}^j_t\right|},\ \text{if } (\mathbf{N}^i,\mathbf{n}^i) < 0,$$

where $\mathbf{q}^i$ is the unit vector in the tangential plane to the contact surface, directed against the relative velocity vector. The boundary conditions take the form

$$\mathbf{u}^i_{\mathbf{n}}(\mathbf{z},t) = \mathbf{u}^j_{\mathbf{n}}(\mathbf{z},t),\ \mathbf{R}^i(\mathbf{z},t) = -\mathbf{R}^j(\mathbf{z},t). \tag{12}$$

The tangential components of velocities are calculated based on the tangential components of the reaction force $\mathbf{T}^i(\mathbf{z},t)$, and their preliminary values $\mathbf{T}^{i*}(\mathbf{z},t)$ are obtained from the second Relation (10). If the magnitude of $|\mathbf{T}^{i*}(\mathbf{z},t)| < k\left|\mathbf{N}^i(\mathbf{z},t)\right|$, then $\mathbf{T}^i(\mathbf{z},t) = k\left|\mathbf{N}^i(\mathbf{z},t)\right|$. Otherwise, the internal forces cannot overcome the frictional forces, and there is no sliding at the interface. In that case, the sliding Condition (12) is replaced by the ideal contact Condition (10).

2.4. Fracture

Kinematic strength characteristics include the limiting values of elongation (usually under uniaxial tension) and shear. Brittle materials are also destroyed by compressive strains. Kinematic characteristics are accumulated quantities incorporating the entire history of the process. The most frequently used quantities are the limiting elongation and shear strain. Finding these quantities involves the calculation of the primary tensile and compressive strains.

$$\varepsilon_1 = \frac{\varepsilon_{xx}+\varepsilon_{yy}}{2} + \sqrt{\left(\frac{\varepsilon_{xx}-\varepsilon_{yy}}{2}\right)^2 + \varepsilon_{xy}^2},$$
$$\varepsilon_2 = \frac{\varepsilon_{xx}+\varepsilon_{yy}}{2} - \sqrt{\left(\frac{\varepsilon_{xx}-\varepsilon_{yy}}{2}\right)^2 + \varepsilon_{xy}^2}$$

and also, the shear strain

$$\varepsilon_\tau = \frac{(\varepsilon_1 - \varepsilon_2)}{2}.$$

If the tensile strains in the course of deformation exceed the limiting elongation ε_1^* (i.e., $\varepsilon_1 > \varepsilon_1^*$) or the limiting shear strain $\varepsilon_\tau > \varepsilon_\tau^*$, ε_τ^*, then the element material is assumed to be fractured, i.e., it has no longer resistance to tension and shear but still has resistance to compression.

Force strength parameters include the limiting values of tensile [29], compressive, and shear stresses. If the stresses proper are used, then they are instantaneous criteria, i.e., as soon as the principal stresses exceed the limiting values, the element material is assumed to be fractured:

$$\begin{cases} \sigma_1 > \sigma_1^*, \\ \sigma_2 > \sigma_2^*, \\ \sigma_\tau = \frac{(\sigma_1-\sigma_2)}{2} > \sigma_\tau^*. \end{cases}$$

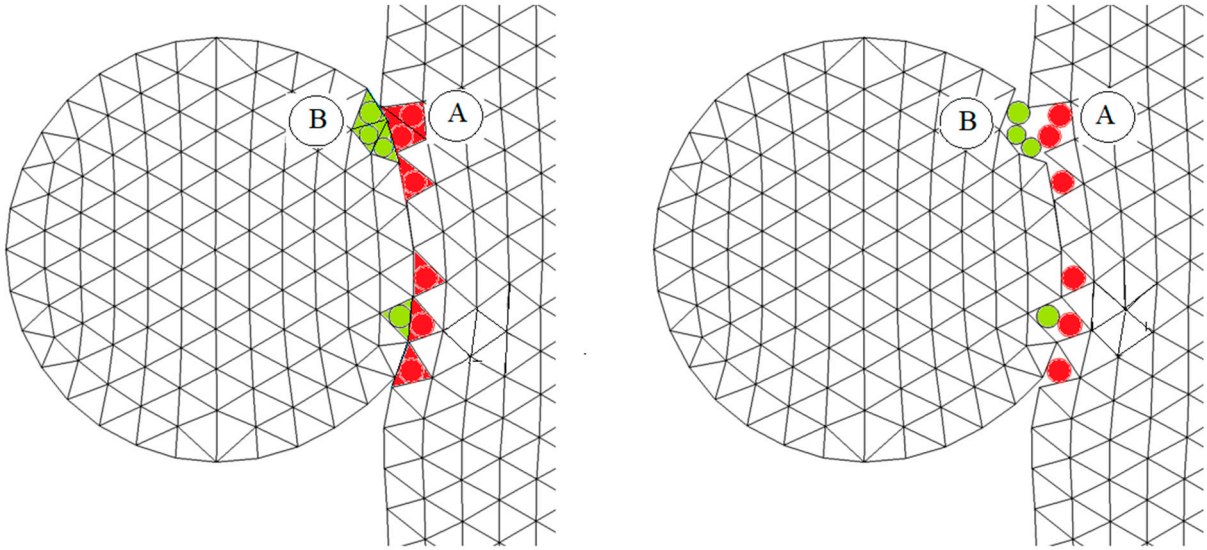
Most materials, however, possess properties of plasticity and viscosity; therefore, their fracture requires a time interval during which the material is under overstrain. The code involves one of such criteria (it is demonstrated by an example of the principal tensile stress) [30]:

$$\sigma_t = \frac{\sum\limits_{i=n_1}^{n_2} (\sigma_1 - \sigma_1^*)_i \Delta t_i}{\sum\limits_{i=n_1}^{n_2} \Delta t_i} > \sigma_t^*, \quad \sigma_1 - \sigma_1^* > 0.$$

2.5. Conversion of Fractured Elements to Particles

If the element is at the boundary of the computational domain and the parameters of the material reach a critical value, the material of the element is replaced by discrete particles. The radius of the particle is calculated from the condition of incorporating one or more of the particles in the element. The mass of the element is allocated between the discrete particles. For a one-time step, only one layer of boundary elements can be converted into discrete particles, so the velocity of the wavefront of destruction does not exceed the speed of disturbances in the medium. Figure 2 shows the conversion of triangle elements (A, B, and others) to particles [31] in the 2D formulation:

- Element A is removed from the element grid;
- Particle A is added as a particle node;
- All of the element variables (stress, strain, damage, etc.) are transferred to the particle;
- The mass, velocity, and center of gravity of the particle node are set to those of the replaced element. The nodal velocity is obtained from the momentum of the element (three nodal masses and velocities);
- The masses of nodes b, c, and k are reduced by the removal of element A;
- For the conversion of element B (which has two sides on the surface) to node B, most of the steps are similar to those used for element A.



(**a**) (**b**)

Figure 2. Conversion of triangle elements to particles. (**a**)—interface nodes and elements before conversion, (**b**)—interface after conversion of elements. The green circles and areas belong to Interacting Body 1, and the red ones to Interacting Body 2.

In the 3D formulation, the algorithm for replacing cells containing damaged material when they reach critical values with discrete particles that simulate the behavior of the destroyed material is identical to the 2D case described above.

The behavior of the shear modulus under pressure and temperature is described in [32]. The model of a heterogeneous environment and the solved problems are presented in [33–35].

3. Propagation of Shock Waves in a Periodically Volume-Reinforced Metal Matrix Composite

The problem of determining effective modules for heterogeneous media dates back to classical works [36,37], while research on shock waves has been conducted in [38,39]. Although this problem has been addressed in many monographs, such as [40,41], it has yet to find a final solution. In [42], a deviation from the rule of mixtures in the shock adiabat was discovered for a volume-reinforced metal matrix composite. As this phenomenon was not observed in our work, for example, in [23,33], we conducted numerical calculations of a volume-reinforced metal matrix composite using averaging according to the methodology outlined in [33]. Figure 3 shows a model of such a composite that we used in our calculations, similar to [18].

Figure 4 displays the calculated dependence of the shock wave velocity on the mass velocity, revealing that the direct numerical modeling of a penetrating heterogeneous medium demonstrates that the shock wave velocity corresponds to the calculation of the shock adiabat of the composite using the additive approach (rule of mixtures), at least at shock wave velocities exceeding C_l, the longitudinal sound speed in the composite, showing deviations from the parameters calculated using the mixture rule of no more than 3%.

Although numerous numerical studies of shock waves were carried out in an interpenetrating composite, we do not present them here as a complete analysis of the shock wave propagation in a periodically volume-reinforced metal matrix composite has already been conducted in [43]; the results of which fully consistent with our calculations. Only one question remains unanswered: the consideration of a reinforced composite fracture under high-speed loading and the influence of the heterogeneous screen structure on this process.

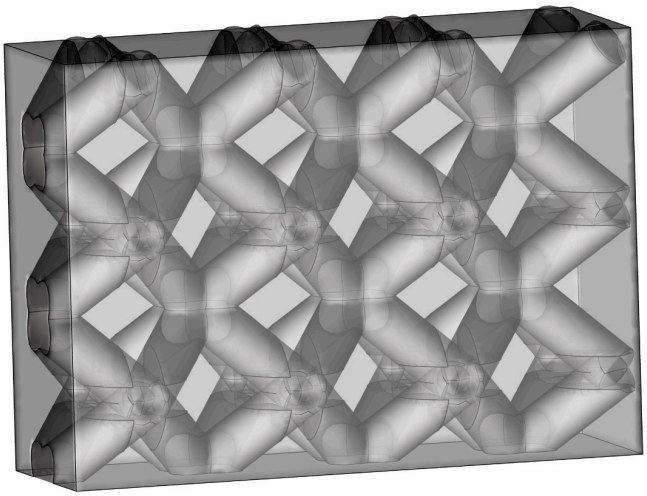


Figure 3. A model of a volume-reinforced composite with an A356 matrix and 316L inclusions.

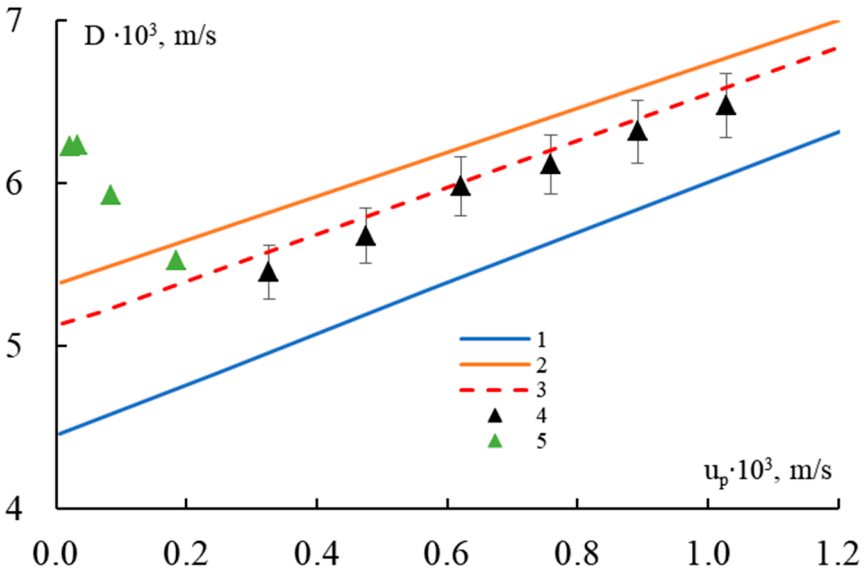


Figure 4. Shock wave velocity vs. the mass velocity: 1—316L steel; 2—A356 aluminum alloy; 3—calculation according to the additive rule of mixtures; 4—direct numerical modeling in a metal matrix composite, 5—C_l.

4. Problem Statement

Our objective is to design a heterogeneous screen to protect critical spacecraft components from space debris particles. We aim to investigate the high-speed interaction between spherical space debris particles and protective screens made of various structures using specified materials. The configuration of the problem is presented in Figure 5, which depicts the reinforced A356 + 316L screen placed in a protective casing to prevent its movement.

To calibrate the parameters of the computational model, we will utilize the work of [18], which provides experimental data on high-speed collisions of aluminum particles with five distinct screens. The numerical simulation of the collision processes permits to identification of the screens that exhibit adequate resilience against space debris particles. Additionally, we consider another three screens that can be produced using selective laser sintering of powders from the same materials as in [18]. The material properties for the aluminum alloys Al2017-T4 and A356 are taken from [44,45] and for steel 316L from [46].

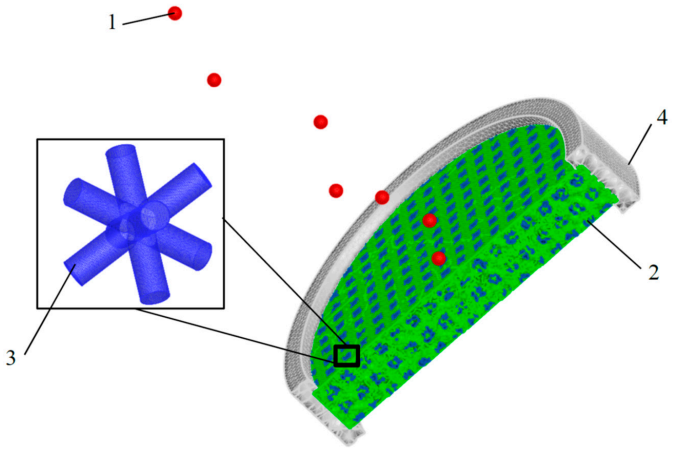


Figure 5. Geometric model: 1—Al2017-T4 spheres; 2—A356/316L volume-reinforced screen; 3—shape of the volume reinforcement; 4—heavy alloy protective casing.

For calculations, we will use the geometric dimensions of the impacting particle and screens from [18]. A spherical particle with a diameter of 1.9 mm made of the aluminum alloy Al2017-T4 with a mass of 10 mg moves at an initial speed of 6.0 km/s in all calculations. Every protective screen, with the exception of screen #2, has the same areal density. We evaluate the following protective screens:

- Screen #1—a steel 316L plate, 4.5 mm thick;
- Screen #2—an A356 aluminum alloy plate, 12.0 mm thick;
- Screen #3—a two-layer plate made of 316L/A356, 7.5 mm thick (3.0/4.5);
- Screen #4—a two-layer plate made of A356/316L, 7.5 mm thick (4.5/3.0);
- Screen #5—a metal-matrix composite plate with the matrix composed of the A356 aluminum alloy and the volume reinforcement made of steel 316L, as is illustrated in Figure 3. The unit volume of the heterogeneous inclusion in such a plate has a face-centered cubic (FCC) symmetry with a side length of 2.5 mm and a diameter of 0.8 mm. The screen thickness is 7.5 mm;
- Screens #6, #7, and #8 are considered later as alternatives;
- Screen #9—A356 aluminum alloy plate, 13.4 mm thick.

The diameter of the protective screens in all calculations is 50.0 mm. Every protective screen, with the exception of screen #2, has the same areal density. All screens are placed in a protective casing to eliminate the influence of free lateral surfaces on the stress state of the screen materials. The effective volumetric concentration of steel in screens #3, #4, and #5 is 38%. The thicknesses and areal densities of the screens are listed in Table 1.

Table 1. Parameters of the considered screens.

Screen	Material of the Screen	Density, g/cm^3	Areal Density, g/cm^2	Thickness, mm
#1 [18]	Stainless steel 316L	8.0	3.6	4.5
#2 [18]	Aluminum alloy A356	2.7	3.24	12.0
#3 [18]	Two-layer composite 316L/A356	4.8	3.6	7.5
#4 [18]	Two-layer composite A356/316L	4.8	3.6	7.5
#5 [18]	Volume-reinforced composite	4.8	3.6	7.5
#6	Uniform distribution of 316L steel grains in an A356 matrix	4.8	3.6	7.5
#7	Direct gradient distribution of 316L steel grains in an A356 matrix	4.8	3.6	7.5
#8	Inverse gradient distribution of 316L steel grains in an A356 matrix	4.8	3.6	7.5
#9	Aluminum alloy A356	2.7	3.6	13.4

5. Material Parameter Calibration

The numerical calculations gave the parameters for the craters (depth, diameter, and volume), which were compared with experimental data for all screens. As the calculated craters had a shape close to an ellipsoid, as seen in Figure 6a, an ellipse with semi-axes a and b was inscribed in the transverse section of the calculated crater to determine its volume by the formula:

$$V_{calc} = \pi \left(\frac{b}{a}\right)^2 h^2 \left(a - \frac{h}{3}\right)$$

In most calculations, an ellipsoid with semi-axes $a = h$ and $b = d/2$ can be inscribed in the crater, and the volume of the crater is calculated using the formula:

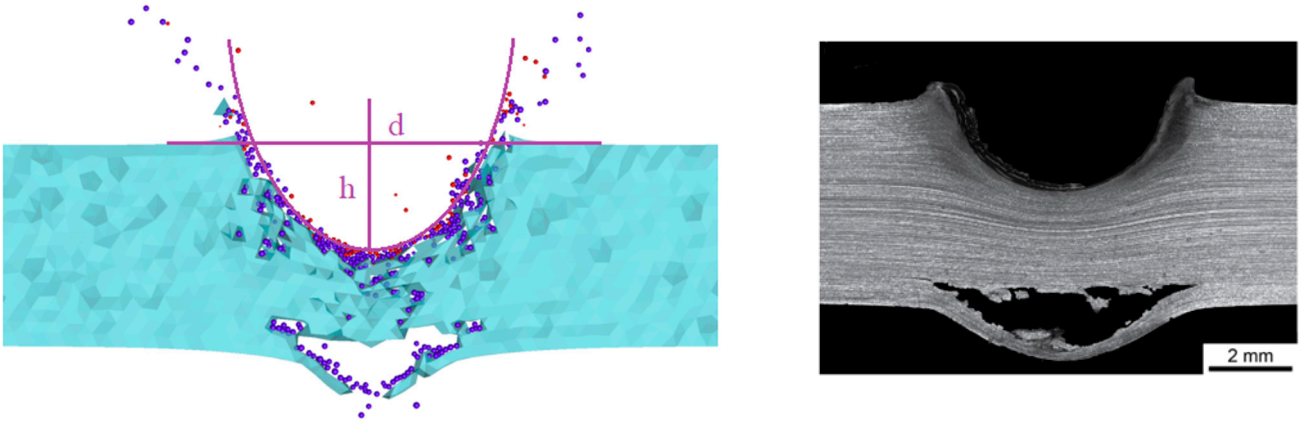
$$V_{calc} = \pi\, h\, d^2/6$$

The results of numerical modeling of the interaction of a spherical particle with screens of different structures were summarized, and the obtained crater parameters were compared with the experimental data from [18]. The experimental data and the results of numerical simulations of the formed craters for all considered screens are presented in Table 2, where h, d, and V are the depth, diameter, and volume of the crater as measured in the experiment, and h_{calc}, d_{calc}, and V_{calc} are the depth, diameter, and volume of the crater as obtained through numerical simulation.

Table 2. Crater size in the screens.

Screen Type	Experiment				Numerical Simulation			
	h, mm	d, mm	V, mm^3	Spall	h_{calc}, mm	d_{calc}, mm	V_{calc}, mm^3	Spall
#1	2.1	5.7	36	spall	2.30	5.60	31	spall
#2	4.5	8.2	158	spall	4.86	7.20	133	spall
#3	2.4	6.4	52	spall	3.70	5.35	55	spall
#4	4.5	8.4	166	no	4.25	7.40	162.6	no
#5	4.7	8.0	55	delamination	3.28	6.38	63	single grain detachment
#6	-	-	-	-	3.20	5.84	54	single grain detachment
#7	-	-	-	-	3.62	6.63	78	no
#8	-	-	-	-	3.01	5.47	39	spall
#9	-	-	-	-	4.67	7.42	134	spall

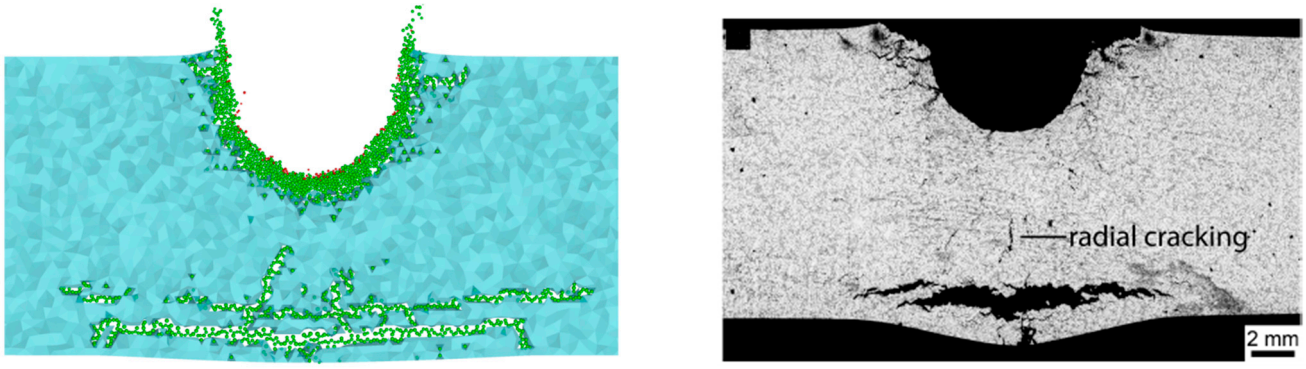
To determine the parameters of the calculated crater, a plate with a thickness of approximately the step of the division of the computational grid was cut out of the screen, passing through the center of the crater. The comparison between the calculated shape of the crater in screen #1, made of 316L steel, and the shape of the experimental crater is presented in Figure 6. Since the "REACTOR 3D" software package uses a hybrid meshless-mesh calculation method, the destroyed material is represented by finite-size particles, differentiated by color in all figures. It is worth noting that the depth of the calculated crater exceeds the depth of the experimental one by approximately 10%, while the calculated diameter almost coincides with the experimental one. However, there is a deviation in the volume of the crater; it reaches 14%. The thickness of the spalled part on the screen's backside is comparable to the experimental thickness.



(**a**) (**b**)

Figure 6. Comparison of the crater shapes in the 316L steel screen #1: (**a**) simulation results; (**b**) optical micrograph of the impact plane in cross-section [18].

The calculated crater in screen #2, made of aluminum alloy A356, was found to be 8% deeper, 12% smaller in diameter, and 16% smaller in volume than the experimental one, as shown in Figure 7. There are cracks on the front side of the screen which allow the "sponges" of the crater to separate from the screen. The thickness of the spall on the screen's backside is slightly smaller than the experimental one. Radial cracks caused by bending deformations are also present, as well as in the experiment.



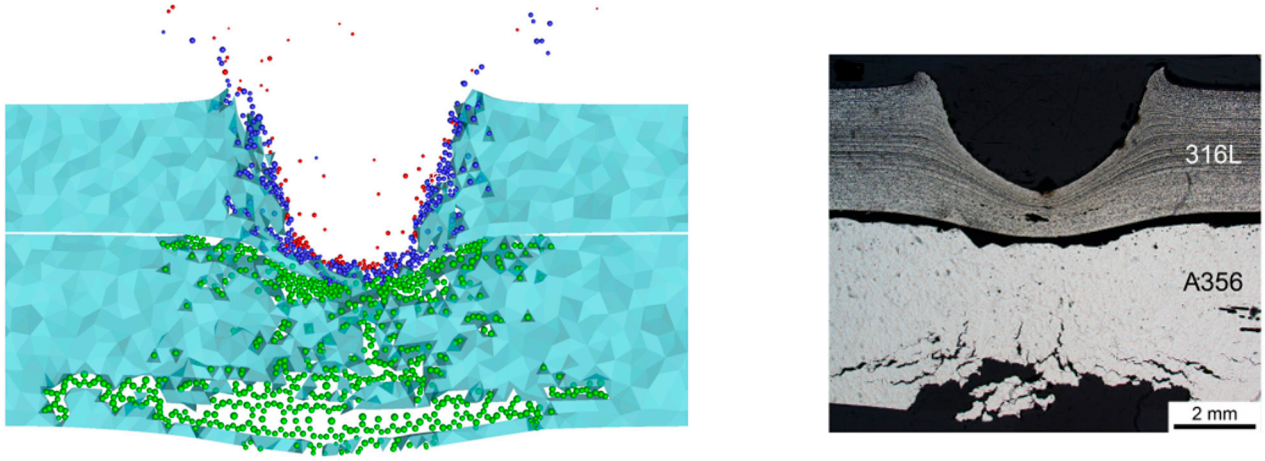
(**a**) (**b**)

Figure 7. Comparison of the crater shapes in screen #2 of the aluminum alloy A356: (**a**) simulation results; (**b**) optical micrograph of the impact plane in cross-section [18].

To ensure consistency in areal density, screen #2, made from A356 aluminum alloy, should possess a thickness of 13.4 mm. We conducted calculations for screen #9 with the required thickness. The calculated crater parameters for screen #9 have values quite close to the experimental values (see Table 2). By increasing the thickness of screen #9 by 1.4 mm compared to screen #2, the depth of the crater decreased while its diameter increased. On a semi-infinite screen, the crater's shape would become hemispherical.

Let us examine a two-layer screen composed of aluminum alloy plates on the front and stainless steel on the back (screen #3). The stainless steel 316L plate is 3 mm thick, while the aluminum alloy A356 plate is 4.5 mm thick. In this case, the calculated crater parameters have several high errors: the depth exceeds the experimental depth by 12.5%, the diameter is smaller by 16.4%, and the volume of the crater exceeds the experimental volume by only 5.8%. Figure 8 shows a comparison of the crater cross-sections. In the calculation, the steel plate sustained significantly more damage compared to the experiment, while the

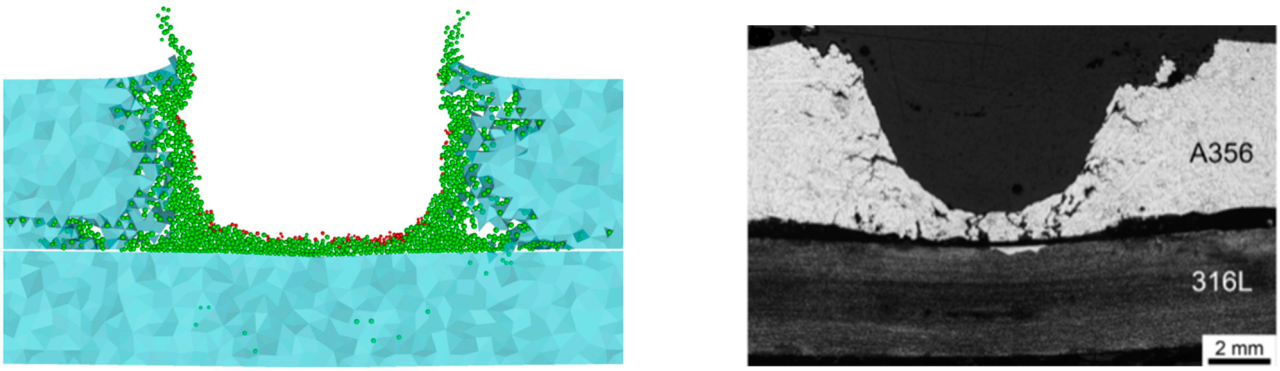
aluminum plate suffered damage and fracture similar to the experimental sample. The only difference is that the plate has a larger diameter but slightly less thickness. It can be concluded that this is the upper limit of the process parameters for material fracture of the screen.



(**a**) (**b**)

Figure 8. Comparison of the crater shapes in screen #3—two-layer protection 316L + A356: (**a**) Simulation results; (**b**) Optical micrograph of the impact plane in cross-section [18].

For screen #4, made up of the A356 alloy plates and 316L steel, the calculated crater depth is 5.6% less than the experimental one, and the diameter is 12% smaller, but the volume of the crater is almost the same as the experimental one, with only a 2.1% deviation. There are no chips in the steel, nor are there any separate particles torn from the back surface. The calculated crater's distinctive feature is its almost cylindrical shape, which is due to the fragile aluminum alloy being crushed on the steel plate, as shown in Figure 9.



(**a**) (**b**)

Figure 9. Comparison of the crater shapes in screen #4—two-layer protection A356 + 316L: (**a**) simulation results; (**b**) optical micrograph of the impact plane in cross-section [18].

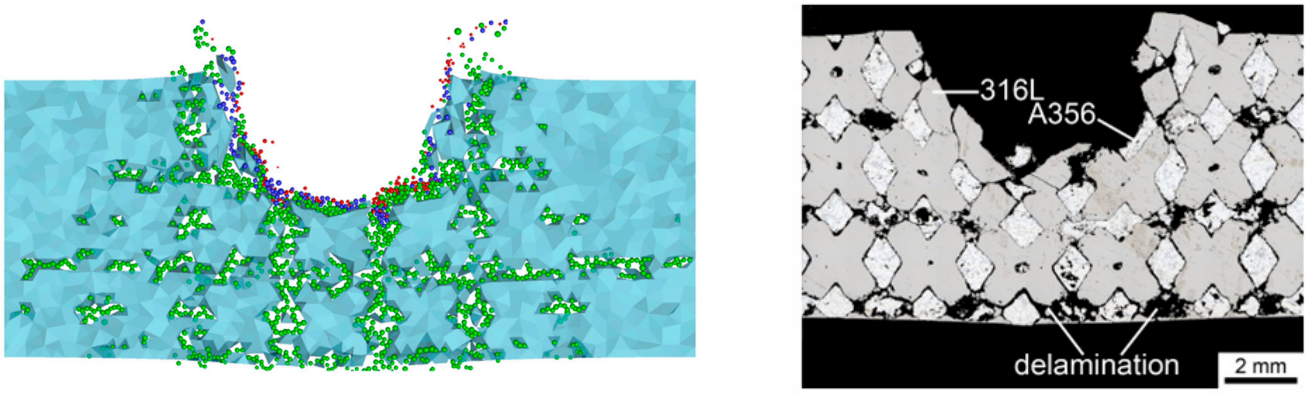
Thus, methodological calibration calculations were carried out using the physical and mechanical properties from [44–46] and experimental data from [18], giving the fracture parameters of homogeneous materials summarized in Table 3.

Table 3. Material parameters.

	K, GPa	G, GPa	C_0, m/s	S	Y, GPa	σ, GPa	ε, %
A356	73.95	26.00	5392	0.270	0.20	0.27	0.045
316L	130.00	79.00	4464	1.544	0.75	2.50	0.05
Al2017-T4	75.71	27.86	5538	1.338	0.28	0.456	0.12

6. Metal Matrix Protective Screens with Interpenetrating Periodic Inclusions

Based on the data obtained, we model a metal matrix reinforced screen with interpenetrating periodic inclusions with an adaptive mesostructure. Numerically constructing such a reinforced screen with volumetric interpenetrating periodic inclusions is a rather complex task. However, it is worth noting that the software package 'REACTOR 3D' allows for the construction of inclusions with an arbitrary 3D shape. In this case, the steel inclusions had the shape of a volumetric cross of four cylinders, as Figures 3 and 5 show. The comparison of the calculated crater's shape to that of the experimental crater in screen #5 is shown in Figure 10. The distinguishing feature of this screen is the stratification between the steel reinforcement and the aluminum matrix. Although there is no macroscopic spall on the backside of the screen, individual grains have been ejected due to spallation processes (refer to Figure 10a). These grains have a very small mass of approximately 0.1 mg and a velocity of around 50–70 m/s, making them an insignificant threat to protected devices.



(**a**) (**b**)

Figure 10. Craters in reinforced screen #5: (**a**) 3D calculation; (**b**) optical microphotograph of the impact plane in cross-section [18].

The calculated shape of the craters in the composite reinforced screen is close to the shape of the craters obtained experimentally. It is worth noting that there are significant discrepancies in the parameters, such as the crater depth, which is 30.2% less than the experimental value, and its diameter, which is 20.2% less than the experimental value. Even with the calculated values of the depth, which is equal to 3.28 mm, and the diameter, which is 6.38 mm, we obtain that the volume of the crater is 14.5% greater than the experimental volume. Apparently, there was a mistake in the parameters of the crater [18].

To quantitatively compare the calculated and experimental crater parameters, the results are tabulated in Table 2, while the deviation in the crater parameters is expressed as a percentage and tabulated in Table 4.

Table 4. Deviation of calculated crater parameters from experimental data.

Error/Screen	#1	#2	#3	#4	#5
Error depth %	9.5	8.0	12.5	5.6	30.2
Error diameter %	1.8	12.2	16.4	11.9	20.2
Error volume %	13.9	15.8	5.8	2.1	14.5

Besides the armor in the form of a volumetric cross of four cylinders, screens reinforced with periodic volumetric inclusions, as shown in Figure 11, were also considered. Discrete steel inclusions in the aluminum matrix in the form of cylinders and spheres (see Figure 11a,b), while maintaining the concentration of components, do not provide adequate protection, as they allow for penetration of the heterogeneous screen, and macroscopic spallation is observed on the backside. Armor screens consisting of "half-crosses" layers (see Figure 11c,d) and lattices (see Figure 11e), while maintaining the concentrations, do not allow for through penetration, but on the back side of such screens, spallation phenomena are observed in the form of the detachment of particles of the A356 aluminum alloy, which have a sufficiently high speed, about 400 m/s, posing a danger to protected devices.

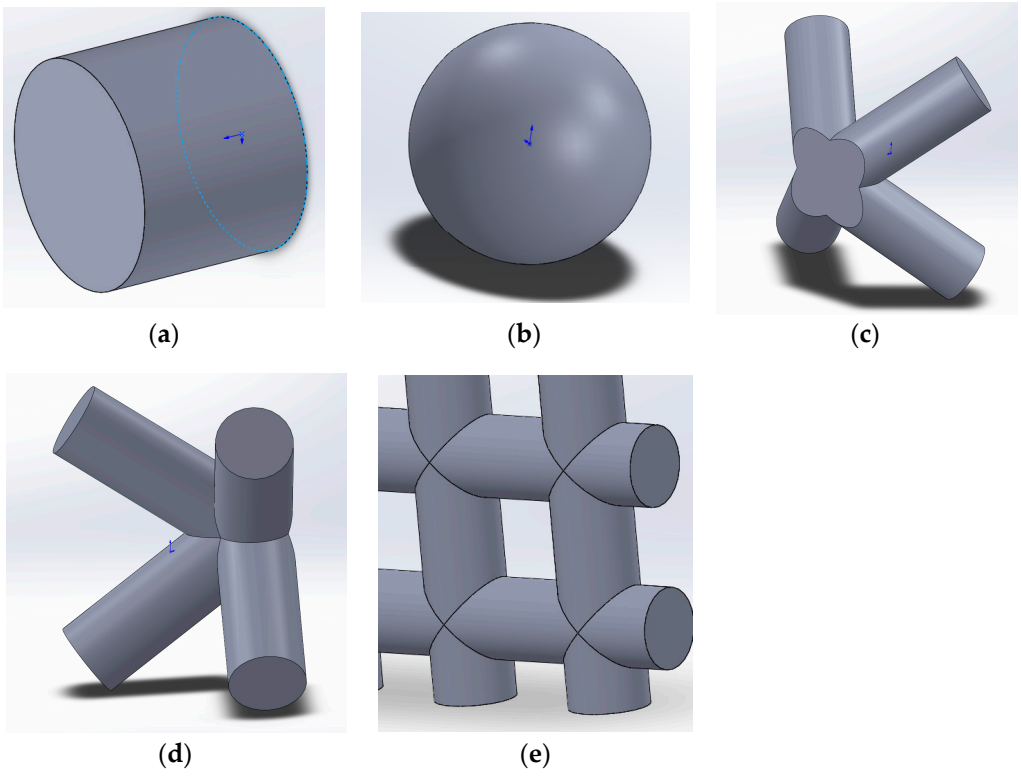
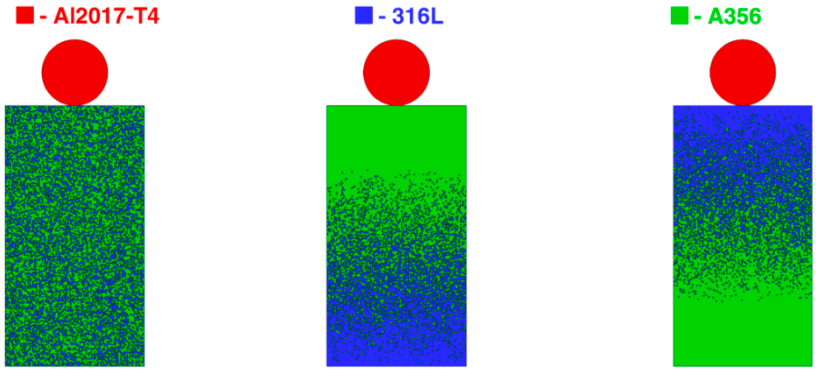


Figure 11. Discrete steel inclusions in the aluminum matrix: (**a**) cylinder; (**b**) sphere; (**c**) straight "half-cross"; (**d**) reverse "half-cross"; (**e**) lattice.

7. Gradient Protective Screens

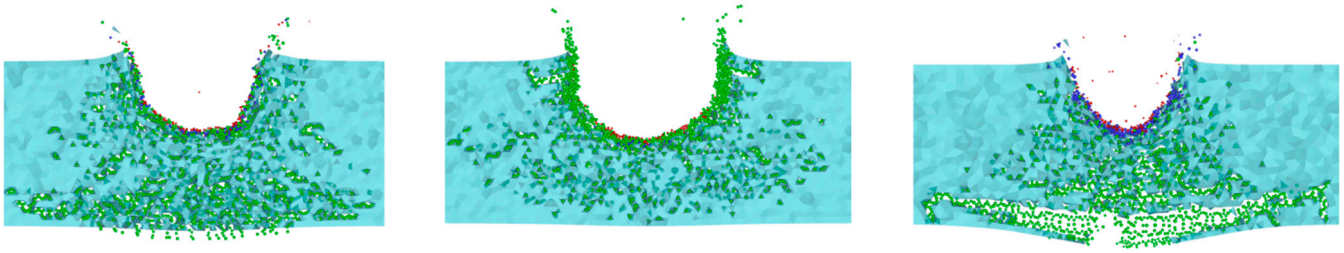
To provide a complete overview of protective screen configurations, we additionally consider the following heterogeneous screens based on the A356 alloy and 316L steel with a volume content of 38% that can be created using existing additive technologies: (1) the screen #6 with a uniform distribution of steel throughout the screen volume (see Figure 12a); (2) the screen #7 with a direct gradient distribution of steel through the screen volume (see Figure 12b); and (3) the screen #8 with a reverse gradient distribution of steel through the screen volume (see Figure 12c). The heterogeneous screens with the gradient steel distribution are similar to layered barriers but with a continuous transition from one material to another without clearly defined boundaries.



(**a**) (**b**) (**c**)

Figure 12. Cross-sections of heterogeneous screens with a steel concentration of 38%: (**a**) Screen #6 with a uniform distribution of 316L steel within the A356 aluminum alloy; (**b**) Screen #7 with a direct gradient distribution of steel; (**c**) Screen #8 with a reverse gradient distribution of steel.

Figure 13 presents the results of the impact loading calculations for spherical particles on the heterogeneous screens. Note that heterogeneous screens behave almost identically to two-layer ones. The uniform distribution of 316L steel in the aluminum matrix increases the effective yield strength, which has a positive effect on the crater volume reduction. However, the presence of aluminum matrix grains on the screen's reverse side leads to the formation of a stream of small particles moving at a speed of 150–250 m/s.



(**a**) (**b**) (**c**)

Figure 13. Calculation results of the interaction between an aluminum sphere and heterogeneous screens. Cross-sections of screens with a thickness equal to the grid step: (**a**) screen #6; (**b**) screen #7; (**c**) screen #8.

Screen #7, which has 100% A356 aluminum alloy on the front side and 100% 316L steel on the back side, has better protective properties than layered screen #4. This is reflected in the calculation of the crater parameters, such as the depth, which is 20% less, the diameter, which is 21% less, and the volume, which is 53% less. As with screen #4, there is no flow of microparticles on the back side, and there is no macroscopic spall.

The behavior of screen #8 closely resembles that of screen #3, as it displays a macroscopic spall with a detached fragment of considerable diameter. The screen volume has suffered significant material damage, particularly near the rear surface.

8. Multiple Impacts of Space Debris Particles

Since the service life of spacecraft is assumed to be 10–20 years, it is natural that protective screens should withstand multiple impacts from SD particles. Let us determine the mass of the incoming SD particles that the armored screen #5 can protect, avoiding penetration. To reduce the number of calculations, it is necessary to predict the maximum

ballistic velocity of the screen from the mass of the incoming particle. Taylor's work [47] proposes a formula for the engineering estimation of the ballistic velocity:

$$\frac{1}{2}m_p V_{bl}^2 = \pi r^2 h Y, \tag{13}$$

where m_p is the particle mass, V_{bl} is the ballistic velocity, r is the hole radius, h is the screen thickness, Y is the yield strength of the screen material.

As the ballistic velocity needs to be evaluated, let us assume that the combination of screen parameters is some constant value. Then, the expression for ballistic velocity is as follows:

$$V_{bl} = \frac{C}{\sqrt{m_p}}, \tag{14}$$

To calibrate the constant C, two or three calculations need to be carried out to determine the ballistic velocity at a given particle mass. In our case, $C \sim 1.01$. Figure 14 illustrates the applicability of this formula and the results of numerical calculations. This Approximation (14) provides a 10% error margin for the calculation.

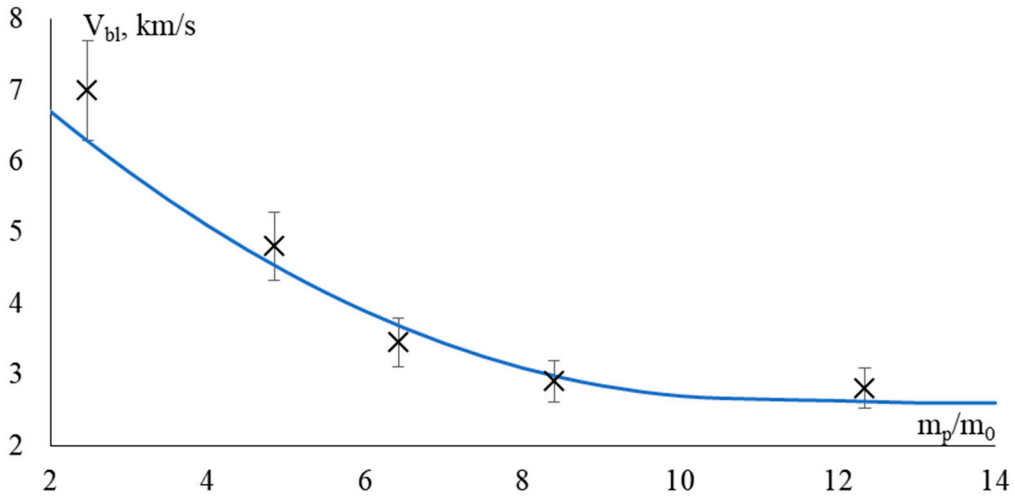
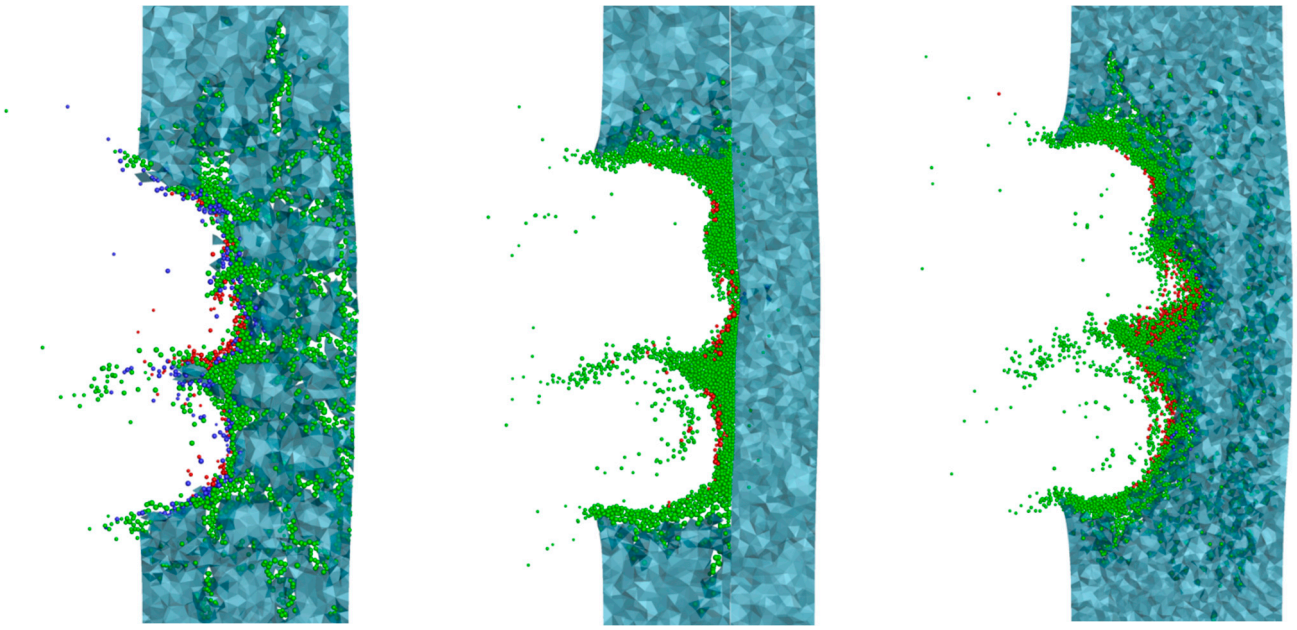


Figure 14. Dependence of the maximum ballistic velocity on the mass of the incoming particle according to the Formula (14). Crosses represent the results of numerical calculations.

Let us perform the calculations for the sequential collision of a group of eight particles with the protective screens, as shown in Figure 5. Random values close to 4 µs were taken as time intervals, and the particles were spatially located in a circle of 0.5 cm radius with the first particle at the center, as is indicated in Figure 12. The most resistant screens were selected for testing, namely, screen #5, which is a composite with volumetric reinforcement; screen #4, which is a layered screen of A356/316L; and screen #7, which is a heterogeneous screen with a direct gradient of 316L steel on an A356 matrix.

The calculation results are presented in Figure 15, which shows cross-sections of protective screens with a thickness of approximately one step of the computational grid cut out from the central region. The sequential multiple impact loading by SD particles leads to the propagation of shock waves through the deformed and partially damaged materials of the screens, resulting in further damage and fracture of the materials. The common feature of all screens is the process of damage and fracture of the A356 aluminum alloy, which is quite brittle. For the volumetrically reinforced composite, delamination between the steel elements and the aluminum matrix is characteristic, as can be seen in Figure 15a, and individual grains appear on the back side of the screen due to spallation processes. The mass of such grains is 0.1 mg, and their velocity is 50–70 m/s, so they do not pose a significant danger to the protected devices.



(**a**) (**b**) (**c**)

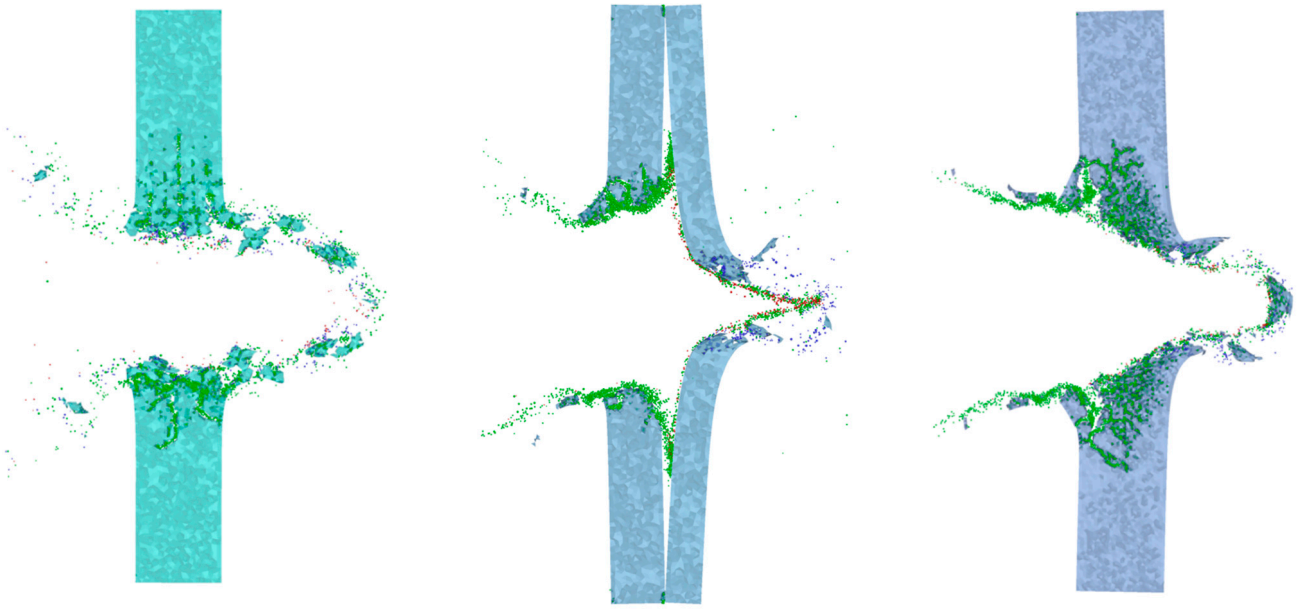
Figure 15. Cross-sectional view of the screens after the impact of a 8 SD particle flow: (**a**) screen #5; (**b**) screen #4; (**c**) screen #7.

The two-layer A356/316L screen withstands a similar impact load because the back side of the screen is made of 316L steel, which has sufficient strength against the spallation. In this case, the size of the crater volume is the largest among the compared protective screens since the A356 aluminum alloy quickly becomes damaged and starts to break down, as shown in Figure 15b. There are no detached microscopic grains behind the barrier since the back side is made of steel.

A heterogeneous screen with a direct gradient of steel has sufficient resistance to the particle flow impact. Since the front side of the screen is made of pure A356 alloy, it is natural that the initial stage of screen deformation resembles that of a layered screen. However, as the process advances into the depth of the screen, the resistance to deformation increases due to the inclusion of 316L steel. Therefore, the main damages and fractures of the screen occur on the front side, and the exit of waves to the back side of the screen does not lead to spall phenomena since the back side of the screen consists of pure 316L steel. However, the damage to the aluminum matrix is present throughout the volume of the screen (see Figure 15c).

As all three screens have practically equal chances of protecting an important element of the spacecraft from both a single SD particle and a particle stream, let us consider the capability of the protective screens to withstand a large SD particle twice the diameter at the same impact velocity. Thus, the mass of the impacting SD particle equals eight masses of the particle used in the experiments and calculations described above. Figure 16 shows the comparison of the results of the calculations of the impact of a large SD particle on the screens. All selected screens have through holes.

Screen #5, made of the volumetrically reinforced composite, has a hole close to a cylindrical shape. Large fragments are the fragments of reinforcing steel, while small fragments are the fragments of the aluminum matrix. The velocity of the large fragments in the head part of the barrier stream reaches 380–400 m/s, while that of the small ones reaches 450–475 m/s. On the periphery of the through cavity, stratifications of the reinforcement and matrix are noticeable due to the large deformations (see Figure 16a).



(**a**) (**b**) (**c**)

Figure 16. The result of numerical modeling for the process of large high-speed SD particles penetrating the screens: (**a**) screen #5, (**b**) screen #4, (**c**) screen #7.

The hole in the two-layer screen #4 has a more complex structure since the front aluminum plate received the main energy of the impacting SD particle, which led to the significant deformation of the material and subsequent damage and fracture. The rear steel plate of the screen was subjected to a weakened impact, which resulted in its bending. The stratification of the plates also allowed the shattered aluminum fragments to move radially, reducing the impact on the steel plate, so the final hole had small dimensions and was only in the central area. The steel damage was present in a small vicinity of the through hole. The fragment velocities in the cloud behind the screen were the same as above (see Figure 16b).

Screen #7 is the heterogeneous screen with a direct distribution of steel in the aluminum matrix and also has a through hole due to the impact of a large SD particle. The front side of the screen suffered significant damage due to the release of strong compression waves on the periphery of the initially formed crater, resulting in the detachment of sufficiently thick layers. Since the screen strength increases with the depth of penetration, a layer with large deflections is formed near the rear surface, and the cavity narrows. Further, the residual mass of the impacting SD particle breaks through the thin steel layer, forming a plug. The velocity of both large and small fragments is approximately 360–380 m/s (see Figure 16c).

9. Conclusions

The development and advancement of technologies for creating materials with specific characteristics, such as additive manufacturing, have broadened the range of applications for complex heterogeneous metal matrix materials. Experimental work on the practical implementation of production technologies for such heterogeneous media surpasses the number of studies on material prediction methods and the level of understanding of their properties under intense dynamic loads. This results in a significant gap when it comes to the practical utilization of heterogeneous materials with predetermined properties.

In our study, a significant stride has been made in comprehending the design of heterogeneous materials through direct numerical modeling of deformation and failure processes in such materials under high-speed loading. Furthermore, we have demonstrated that:

1. For the first time, taking into account the fracture effects, a numerical solution has been obtained for the problem of high-velocity interaction between space debris

particles and a volumetrically reinforced penetrating composite screen. It has been demonstrated that the screens constructed as two-layer A356/316L screens, volume-reinforced composites, and heterogeneous screens with a direct gradient distribution of steel in an aluminum matrix provide protection to devices from both individual space debris particles and streams of debris particles moving at speeds up to 6.0 km/s.

2. The physico-mechanical parameters of the heterogeneous material behind the shock wave front, obtained through numerical calculations, show deviations from the parameters calculated using the mixture rule of no more than 3%.
3. It has been shown that reinforcing the aluminum matrix with discrete steel inclusions within the specified mass and dimensional parameters of the screens does not provide sufficient protection for spacecraft components against high-velocity space debris particles.

Author Contributions: Conceptualization, I.S. and E.K.; software, E.K.; validation, A.K. and I.S.; writing—original draft preparation, A.K. and I.S.; writing—review and editing, A.B., I.S. and E.K.; supervision, E.K.; project administration, A.B.; funding acquisition, E.K. All authors have read and agreed to the published version of the manuscript.

Funding: This research was funded by Russian Science Foundation, project number 23-29-00777, available at https://rscf.ru/en/project/23-29-00777/ (accessed on 1 June 2023).

Institutional Review Board Statement: Not applicable.

Informed Consent Statement: Not applicable.

Data Availability Statement: Not applicable.

Conflicts of Interest: The authors declare no conflict of interest.

References

1. Smirnov, N.N. *Space Debris*; Smirnov, N.N., Ed.; CRC Press: London, UK, 2001; ISBN 9781482288193.
2. Anz-Meador, P.D.; Opiela, J.N.; Shoots, D.; Liou, J.-C. *History of On-Orbit Satellite Fragmentations*, 15th ed.; NASA: Houston, TX, USA, 2018.
3. Whipple, F.L. Meteorites and Space Travel. *Astron. J.* **1947**, *52*, 131. [CrossRef]
4. Christiansen, E.L.; Crews, J.L.; Williamsen, J.E.; Robinson, J.H.; Nolen, A.M. Enhanced Meteoroid and Orbital Debris Shielding. *Int. J. Impact Eng.* **1995**, *17*, 217–228. [CrossRef]
5. Zhuang, S.; Ravichandran, G.; Grady, D.E. An Experimental Investigation of Shock Wave Propagation in Periodically Layered Composites. *J. Mech. Phys. Solids* **2003**, *51*, 245–265. [CrossRef]
6. Grujicic, M.; Pandurangan, B.; Bell, W.C.; Bagheri, S. Shock-Wave Attenuation and Energy-Dissipation Potential of Granular Materials. *J. Mater. Eng. Perform.* **2012**, *21*, 167–179. [CrossRef]
7. Lamberson, L. Investigations of High Performance Fiberglass Impact Using a Combustionless Two-Stage Light-Gas Gun. *Procedia Eng.* **2015**, *103*, 341–348. [CrossRef]
8. Rawal, S.P. Metal-Matrix Composites for Space Applications. *JOM* **2001**, *53*, 14–17. [CrossRef]
9. Kok, Y.; Tan, X.P.; Wang, P.; Nai, M.L.S.; Loh, N.H.; Liu, E.; Tor, S.B. Anisotropy and Heterogeneity of Microstructure and Mechanical Properties in Metal Additive Manufacturing: A Critical Review. *Mater. Des.* **2018**, *139*, 565–586. [CrossRef]
10. DebRoy, T.; Wei, H.L.; Zuback, J.S.; Mukherjee, T.; Elmer, J.W.; Milewski, J.O.; Beese, A.M.; Wilson-Heid, A.; De, A.; Zhang, W. Additive Manufacturing of Metallic Components–Process, Structure and Properties. *Prog. Mater. Sci.* **2018**, *92*, 112–224. [CrossRef]
11. Filippov, A.A.; Fomin, V.M.; Buzyurkin, A.E.; Kosarev, V.F.; Malikov, A.G.; Orishich, A.M.; Ryashin, N.S. The Development of Heterogeneous Materials Based on Ni and B 4 C Powders Using a Cold Spray and Stratified Selective Laser Melting Technologies. *J. Phys. Conf. Ser.* **2018**, *946*, 012005. [CrossRef]
12. Fomin, V.M.; Golyshev, A.A.; Malikov, A.G.; Orishich, A.M.; Filippov, A.A. Creation of a functionally gradient material by the selective laser melting method. *J. Appl. Mech. Tech. Phys.* **2020**, *61*, 878–887. [CrossRef]
13. Fomin, V.M.; Golyshev, A.A.; Kosarev, V.F.; Malikov, A.G.; Orishich, A.M.; Filippov, A.A. Deposition of Cermet Coatings on the Basis of Ti, Ni, WC, and B4C by Cold Gas Dynamic Spraying with Subsequent Laser Irradiation. *Phys. Mesomech.* **2020**, *23*, 291–300. [CrossRef]
14. Zhang, M.; Yu, Q.; Liu, Z.; Zhang, J.; Tan, G.; Jiao, D.; Zhu, W.; Li, S.; Zhang, Z.; Yang, R.; et al. 3D Printed Mg-NiTi Interpenetrating-Phase Composites with High Strength, Damping Capacity, and Energy Absorption Efficiency. *Sci. Adv.* **2020**, *6*, eaba5581. [CrossRef]
15. Pawlowski, A.E.; Splitter, D.A.; Muth, T.R.; Shya, A.; Carver, J.K.; Dinwiddie, R.B.; Elliott, A.M. Producing Hybrid Metal Composites by Combining Additive Manufacturing and Casting. *Adv. Mater. Process.* **2017**, *175*, 16–21.

16. Pawlowski, A.E.; Cordero, Z.C.; French, M.R.; Muth, T.R.; Keith Carver, J.; Dinwiddie, R.B.; Elliott, A.M.; Shyam, A.; Splitter, D.A. Damage-Tolerant Metallic Composites via Melt Infiltration of Additively Manufactured Preforms. *Mater. Des.* **2017**, *127*, 346–351. [CrossRef]
17. Moustafa, A.R.; Dinwiddie, R.B.; Pawlowski, A.E.; Splitter, D.A.; Shyam, A.; Cordero, Z.C. Mesostructure and Porosity Effects on the Thermal Conductivity of Additively Manufactured Interpenetrating Phase Composites. *Addit. Manuf.* **2018**, *22*, 223–229. [CrossRef]
18. Poole, L.L.; Gonzales, M.; French, M.R.; Yarberry, W.A.; Moustafa, A.R.; Cordero, Z.C. Hypervelocity Impact of PrintCast 316L/A356 Composites. *Int. J. Impact Eng.* **2020**, *136*, 103407. [CrossRef]
19. French, M.R.; Yarberry, W.A., III; Pawlowski, A.E.; Shyam, A.; Splitter, D.A.; Elliott, A.M.; Carver, J.K.; Cordero, Z.C. Hypervelocity Impact of Additively Manufactured A356/316L Interpenetrating Phase Composites. In Proceedings of the Solid Freeform Fabrication 2017: Proceedings of the 28th Annual International Solid Freeform Fabrication Symposium—An Additive Manufacturing Conference Hypervelocity, Austin, TX, USA, 7–9 August 2017.
20. Cheng, J.; Gussev, M.; Allen, J.; Hu, X.; Moustafa, A.R.; Splitter, D.A.; Shyam, A. Deformation and Failure of PrintCast A356/316L Composites: Digital Image Correlation and Finite Element Modeling. *Mater. Des.* **2020**, *195*, 109061. [CrossRef]
21. Kraus, A.E.; Kraus, E.I.; Shabalin, I.I. Numerical Simulation of the High-Speed Interaction of a Spherical Impactor with a System of Spaced Heterogeneous Plates. *J. Phys. Conf. Ser.* **2019**, *1404*, 012026. [CrossRef]
22. Kraus, A.E.; Kraus, E.I.; Shabalin, I.I. Impact Resistance of Ceramics in a Numerical Experiment. *J. Appl. Mech. Tech. Phys.* **2020**, *61*, 847–854. [CrossRef]
23. Kraus, A.E.; Kraus, E.I.; Shabalin, I.I.; Buzyurkin, A.E. Evolution of a Short Compression Pulse in a Heterogeneous Elastoplastic Medium. *J. Appl. Mech. Tech. Phys.* **2021**, *62*, 475–483. [CrossRef]
24. Kraus, A.E.; Kraus, E.I.; Shabalin, I.I. Reactor 3D Software Performance on Penetration and Perforation Problems. In *Behavior of Materials under Impact, Explosion, High Pressures and Dynamic Strain Rates*; Orlov, M.Y., Visakh, P.M., Eds.; Springer International Publishing: Berlin/Heidelberg, Germany, 2023; pp. 83–101.
25. Fomin, V.M.; Gulidov, A.I.; Sapozhnikov, G.A.; Shabalin, I.I. *High-Velocity Solids Interaction*; SB RAS: Novosibirsk, Russia, 1999; ISBN 5-7692-0237-8.
26. Wilkins, M.L. *Computer Simulation of Dynamic Phenomena*; Scientific Computation; Springer: Berlin/Heidelberg, Germany, 1999; ISBN 978-3-642-08315-0.
27. Kraus, E.I.; Shabalin, I.I. A Few-Parameter Equation of State of the Condensed Matter. *J. Phys. Conf. Ser.* **2016**, *774*, 012009. [CrossRef]
28. Kraus, E.; Shabalin, I. Melting behind the Front of the Shock Wave. *Therm. Sci.* **2019**, *23*, 519–524. [CrossRef]
29. Maenchen, G.; Sack, E. The Tensor Code. In *Methods in Computational Physics, v.3, Fundamental Methods in Hydrodynamics*; Alder, B., Fernbach, S., Rotenberg, M., Eds.; Academic Press: New York, NY, USA, 1964; p. 221.
30. Tuler, F.R.; Butcher, B.M. A Criterion for the Time Dependence of Dynamic Fracture. *Int. J. Fract. Mech.* **1968**, *4*, 322–328. [CrossRef]
31. Johnson, G.R.; Stryk, R.A. Conversion of 3D Distorted Elements into Meshless Particles during Dynamic Deformation. *Int. J. Impact Eng.* **2003**, *28*, 947–966. [CrossRef]
32. Kraus, E.I.; Shabalin, I.I. A New Model to Determine the Shear Modulus and Poisson's Ratio of Shock-Compressed Metals up to the Melting Point. *High Press. Res.* **2021**, *41*, 353–365. [CrossRef]
33. Kraus, E.I.; Shabalin, I.I.; Shabalin, T.I. Numerical Analysis of Wave Propagation in a Cermet Composite. In *AIP Conference Proceedings*; AIP Publishing LLC: New York, NY, USA, 2017; Volume 1893, p. 030130.
34. Kraus, A.E.; Kraus, E.I.; Shabalin, I.I. Simulation of a Group Impact on a Heterogeneous Target of Finite Thickness. *J. Sib. Fed. Univ. Math. Phys.* **2021**, *14*, 1–12. [CrossRef]
35. Kraus, A.E.; Kraus, E.I.; Shabalin, I.I. A Heterogeneous Medium Model and Its Application in a Target Perforation Problems. In *Multiscale Solid Mechanics. Advanced Structured Materials*; Altenbach, H., Eremeyev, V.A., Igumnov, L.A., Eds.; Springer: Berlin/Heidelberg, Germany, 2021; Volume 141, pp. 289–304.
36. Hashin, Z. The Elastic Moduli of Heterogeneous Materials. *J. Appl. Mech.* **1962**, *29*, 143–150. [CrossRef]
37. Hashin, Z.; Rosen, B.W. The Elastic Moduli of Fiber-Reinforced Materials. *J. Appl. Mech.* **1964**, *31*, 223–232. [CrossRef]
38. Dremin, A.N.; Karpukhin, I.A. Method of Determining the Shock Adiabats for Disperse Materials. *Zh. Prikl. Mekh. I Tekh. Fiz.* **1960**, *1*, 184–188.
39. Duvall, G.E.; Taylor, S.M. Shock Parameters in a Two Component Mixture. *J. Compos. Mater.* **1971**, *5*, 130–139. [CrossRef]
40. Bakhvalov, N.; Panasenko, G. *Homogenisation: Averaging Processes in Periodic Media*; Mathematics and its Applications; Springer: Dordrecht, The Netherlands, 1989; Volume 36, ISBN 978-94-010-7506-0.
41. Christensen, R.M. *Mechanics of Composite Materials*; Dover Publications: Mineola, NY, USA, 2005; ISBN 978-0486442396.
42. Poole, L.L.; Gonzales, M.; Moustafa, A.R.; Gerlt, A.R.C.C.; Cordero, Z.C. Shock Dynamics in Periodic Two-Dimensional Composites. In *AIP Conference Proceedings*; American Institute of Physics Inc.: Melville, NY, USA, 2020; Volume 2272, p. 120020.
43. Taylor, S.V.; Gonzales, M.; Cordero, Z.C. Shock Response of Periodic Interpenetrating Phase Composites. *APL Mater.* **2022**, *10*, 111119. [CrossRef]
44. Baluch, A.H.; Park, Y.; Kim, C.G. High Velocity Impact Characterization of Al Alloys for Oblique Impacts. *Acta Astronaut.* **2014**, *105*, 128–135. [CrossRef]

45. Kim, Y.H.; Lee, S.; Kim, N.J.; Cho, K.M. Effect of Microstructure on the Tensile and Fracture Behavior of Cast A356 AlSiCp Composite. *Scr. Metall. Mater.* **1994**, *31*, 1629–1634. [CrossRef]
46. Hixson, R.S.; McQueen, R.G.; Fritz, J.N. The Shock Hugoniot of 316 SS and Sound Velocity Measurements. In *AIP Conference Proceedings*; AIP: Melville, NY, USA, 1994; Volume 309, pp. 105–108.
47. Taylor, G.I. The Formation and Enlargement of a Circular Hole in a Thin Plastic Sheet. *Q. J. Mech. Appl. Math.* **1948**, *1*, 103–124. [CrossRef]

Disclaimer/Publisher's Note: The statements, opinions and data contained in all publications are solely those of the individual author(s) and contributor(s) and not of MDPI and/or the editor(s). MDPI and/or the editor(s) disclaim responsibility for any injury to people or property resulting from any ideas, methods, instructions or products referred to in the content.